Computational Mechanistic Insights into Reversible and Irreversible Covalent Inhibitors Targeting SARS-CoV-2 M^{pro}

Mojgan Asadi,[1,2] Ashim Nandi, [1] and Arieh Warshel[1,*]

[1]Department of Chemistry, University of Southern California, Los Angeles, California 90089-1062, United States

[2]Department of Chemistry, Stanford University, Stanford, California 94305-5012, United States

*Correspondence: warshel@usc.edu

Abstract

The treatment of SARS-CoV-2 can be accomplished by an effective suppression of its 3CL protease ($3CL^{pro}$), also known as the main protease (M^{pro}) and nonstructural protein 5 (nsp5). Covalent inhibitors can irreversibly and selectively disable the protease, particularly when they are highly exothermic. Herein we delve into the distinct kinetic behaviors exhibited by two covalently linked SARS-CoV-2 inhibitors. One of these inhibitors features a nitrile reactive group, while the other has this group replaced by an alkyne group, a less reactive electrophile. Our investigations involve the assessment of pertinent free energy surfaces through the utilization of both ab initio and empirical valence bond (EVB) simulations. The calculated free energy profiles show that substituting the nitrile group with alkyne significantly increases the overall reaction exothermicity. This leads to an efficient inhibition, even though the reaction of the nitrile group has a substantially lower barrier than the alkyne group. We examine the time-dependence of IC50 inhibition by applying a novel kinetic simulation approach, which is particularly important in studies of covalent inhibitors with a very exothermic bonding step. Our computational approach reproduces the observed binding kinetics and appears to provide a powerful tool for studies of covalent inhibitors.

Introduction

The coronavirus disease 2019 (COVID-19), caused by the severe acute respiratory syndrome coronavirus 2 (SARS-CoV-2), has been one of the most devastating pandemics of recent times. There has been significant effort to develop antiviral therapeutics targeting two proteases of SARS-CoV-2: the main protease (M^{pro}) and papain-like protease (PL^{pro}).[1–3] Out of these targets, M^{pro}, also known as 3-chymotrypsin-like protease ($3CL^{pro}$), has received significant attention in the development of antivirals, i.e., protease inhibitors, to combat COVID-19,[4–7] with the fundamental aim to disrupt the function and life cycle of SARS-CoV-2.[8] Several small-molecule inhibitors of SARS-CoV-2 M^{pro} have been discovered, with a few progressing into early-phase human clinical trials.[9,10] Covalent enzyme inhibitors are of significant interest as biochemical tools and therapeutic drugs. Previous authors have summarized the distinctive advantages and disadvantages of covalent enzyme inhibition in drug and inhibitor design.[11–13] As the treatment of COVID-19 requires disabling the activity of M^{pro}, covalent inhibitors with high exothermicity and irreversible binding to M^{pro} can be important candidates for antiviral treatments. A notable therapeutic strategy for COVID-19 is to design inhibitors with an electrophilic reactive group ("warhead") that binds to the nucleophilic target cysteine 145 (Cys145) in M^{pro}. Cys145 is essential for the catalytic activity of M^{pro}, so blockage or modification of this residue is detrimental to the virus.[14–18] Nirmatrelvir is a new FDA-approved medication developed for the treatment of COVID-19[19] that has a nitrile warhead and binds covalently and reversibly to Cys145. There are several known derivatives of nirmatrelvir, some of which are reversible, while others lead to irreversible catalytic reactions.

Recently, Zhang and co-workers have demonstrated the effectiveness of latent electrophilic warheads,[20], such as terminal alkynes, in inhibiting M^{pro} compared to more reactive electrophiles like acrylamides. These terminal alkyne warheads demonstrate marked specificity for M^{pro} due to their lack of intrinsic reactivity, which circumvents nonspecific binding to other cellular proteins. Upon activation within M^{pro}'s active site, these warheads have shown potent inhibition, as confirmed through biochemical assays and structural analysis via X-ray crystallography. Notably, these terminal alkyne-based inhibitors have also exhibited promising antiviral activity in cellular models of COVID-19, indicating their potential as effective therapeutic agents.

Our prior computational investigations into covalent inhibitors targeting M^{pro} explored the mechanism of α-ketoamide inhibitors[18] and the estimation of their absolute binding free energies.[21] This study centers on a comparative analysis between nirmatrelvir and its alkyne-substituted counterpart, where the nitrile group is substituted with an alkyne group[22,23] (see Figure 1). Our objective is to elucidate the underlying factors responsible for the disparate behavior exhibited by these inhibitors, particularly with regard to the time-dependent inhibition process. To achieve this goal, we conducted a comprehensive exploration of the reaction mechanisms associated with each inhibitor through ab initio and empirical valence bond (EVB) simulations. A prior experimental study[20] has shown that the alkyne derivative inhibits M^{pro} approximately five times less effectively than nirmatrelvir, with an IC50 value of ~0.76 μM for nirmatrelvir and IC50 ≥ 0.063 μM for the alkyne derivative, following a preincubation period of three hours.[22,24] Our simulations have not only substantiated the exothermic nature of the alkyne substitution but also replicated the corresponding time-dependent IC50 trend, corroborating the assertion that the alkyne derivative is a more potent inhibitor compared to nirmatrelvir.

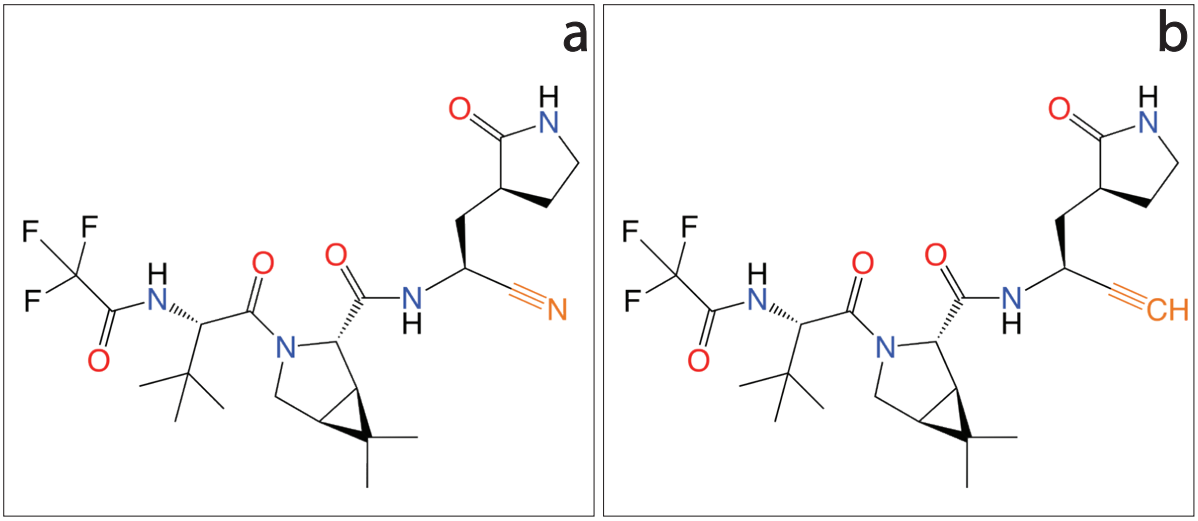

Figure 1: Chemical structure for nirmatrelvir (a) and its alkyne derivative (b), in which the nitrile reactive group is substituted with an alkyne group.

Computational Methods

System Equilibration

Our study began with the utilization of a co-crystal structure of the main protease (M^{pro}) of SARS-CoV-2 and the drug nirmatrelvir. The specific structure employed was sourced from the Protein Data Bank (PDB), under the identifier 7RFS.[24] In this structure, nirmatrelvir is observed to be covalently bonded to the cysteine residue at position 145 (Cys145) of the protease. To investigate the effects of an alkyne derivative, we referenced a similar co-crystal structure wherein the derivative forms a covalent bond at the same cysteine residue, as detailed in the study by Zhang et al. (PDB 8FY6).[20] Following the selection of the initial structures, we performed molecular dynamics simulations using the GROMACS software suite (version 2021)[25] with 40 ns trajectories. The Amber force field (ff14sb) was employed to model the interactions within the system. Subsequently, we carefully selected suitable initial configurations from the simulation trajectories to serve as starting points for the subsequent calculations involving the empirical valence bond (EVB) method. In order to define the force field parameters for the ligand atoms, we referred to the generalized Amber force field (GAFF) using AmberTools 21.[26]

Ab initio Calculations

The reaction mechanisms pertinent to the aqueous phase, crucial for the calibration of EVB study (see below) were explored using ab initio computational methods. The study entailed modifying the inhibitor molecules under consideration by truncating their reactive groups and capping the resulting sites with a methane moiety, as depicted in Figures S1 and S2 in the Supplementary Information section. For the computational analysis, we employed the Gaussian 16 software package.[27] The quantum mechanical calculations were executed using Density Functional Theory (DFT), specifically applying the M06-2X functional combined with the 6-311+G(d,p) basis set to ensure a balance of computational efficiency and accuracy.[28–31] Additionally, the conductor-like polarizable continuum model (CPCM)[32] was utilized to simulate solvent effects within these calculations. Both the geometry optimizations and energy evaluation were conducted under this theoretical framework.

EVB Simulations

The EVB methodology utilizes a hybrid quantum mechanics/molecular mechanics (QM/MM) framework to model chemical reactions through a combination of relevant diabatic states. This enables an efficient exploration of reaction processes,[33,34] as detailed in the Supplementary Information. Prior studies have validated the utility of EVB in analyzing protease inhibition thermodynamics.[18,35–38]

Our EVB calculations were executed with the Q6 simulation software package.[39] Within these simulations, the active site of the reaction—comprising the inhibitor's reactive groups, Cys145, His41, and a catalytic water molecule in nitrile—was designated as region 1. The remainder of the enzyme-solvent system was categorized as region 2. Electrostatic potential (ESP) charges for atoms in region 1 were derived from Gaussian 16 calculations,[27] which were then transformed into Restrained Electrostatic Potential (RESP) charges using the Antechamber tool from AmberTools 21.[26] The initial position of the sulfur in cysteine was used to set the center of the simulations sphere. The system was immersed in a water sphere with a diameter of 25 Å, where the water molecules were described by the TIP3P model[40] and subjected to the SCAAS boundary conditions,[41] where the long-range effects were treated by the local reaction field.[42]

The multi-stage optimization of each reaction step commenced with a local energy minimization, constraining all heavy atoms with a force constant of 20 kcal/ (mol $Å^2$), followed by a gradual relaxation of these restraints and a temperature increase from 5 to 300 K over 1 ns for system equilibration. Subsequent to this, free-energy perturbation/umbrella sampling (FEP/US)[43] simulations were conducted on the equilibrated systems to obtain the free-energy profiles. Ab initio activation and reaction energy data from reference solution reactions were then employed to fine-tune the EVB Hamiltonian for each step of the reaction mechanism. For comprehensive sampling, we performed five umbrella sampling replicas, each comprising 100 frames with a 5 ps duration per frame to ensure statistical reliability and robustness of the results.

Time-dependent kinetic simulations

In the case of very exothermic covalent inhibitors, the justification of the use of the standard kinetic assay equations is far from obvious. Thus we used a kinetic simulation to evaluate the time

dependence of the competitive inhibition of M^{pro} in the experimental assay conditions by solving the first-order system of equations as described in ref[35], with the exception that the inhibitor may be reversible. That is, competitive inhibition is described by the scheme,

$$\mathrm{E} + \mathrm{S} \underset{k_{-s}}{\overset{k_s}{\rightleftharpoons}} \mathrm{E} \cdot \mathrm{S} \xrightarrow{k_{s,\mathrm{cat}}} \mathrm{E} + \mathrm{P}$$

$$\mathrm{E} + \mathrm{I} \underset{k_{-1}}{\overset{k_1}{\rightleftharpoons}} \mathrm{E} \cdot \mathrm{I}^* \underset{k_{-2}}{\overset{k_2}{\rightleftharpoons}} \mathrm{EI}$$

where E is the enzyme, S is the substrate, P is the product, I and I^* are the free and bound inhibitors, and EI is the covalently bound enzyme-inhibitor complex. The equilibrium constant $K_\mathrm{i} = k_{-\mathrm{s}}/k_\mathrm{s}$, and catalytic rate $k_{\mathrm{s,cat}}$ of the substrate are determined by experimental characterization of the enzyme. The equilibrium constant $K_i = k_{-1}/k_1$ is determined from the calculated PDLD/S-LRA/β binding affinity,[44] ΔG_{bind} by $K_i = e^{\Delta G_{\mathrm{bind}}/k_b T}$ M, while the rates k_2 and k_{-2} are determined from the barrier and reverse barrier, respectively, in the EVB profile using the Arrhenius relation. As the second step of the inhibition scheme is the covalent and possibly irreversible step, k_2 is equivalently denoted as k_{inact}.

Results and Discussion

The key residues of M^{pro} include Cys145, His41, His163, His172, Glu166, and Ser144 (Figure 2) in its active site, which together form the oxyanion hole for the covalent and non-covalent binding interactions. The catalytic dyad Cys145-His41, in which the Nε2 atom of His41 is 3.6Å away from the SG atom of Cys145, participates in the first proton transfer. We initially observed that the protonation state of His163 plays a crucial role in catalytic activity and binding affinity. One possible rationale is that the position of carbonyl oxygen in pyrrolidin-2-one of the inhibitors is stabilized by hydrogen bonding with His163. Thus, we proceeded with our calculations assuming Nε2 in His163 is protonated. We explored different ionizable states of His164 and His172 and overall, we found no significant changes in the EVB energy barrier when changing the protonated nitrogen from Nε2 to Nδ1 or to both.

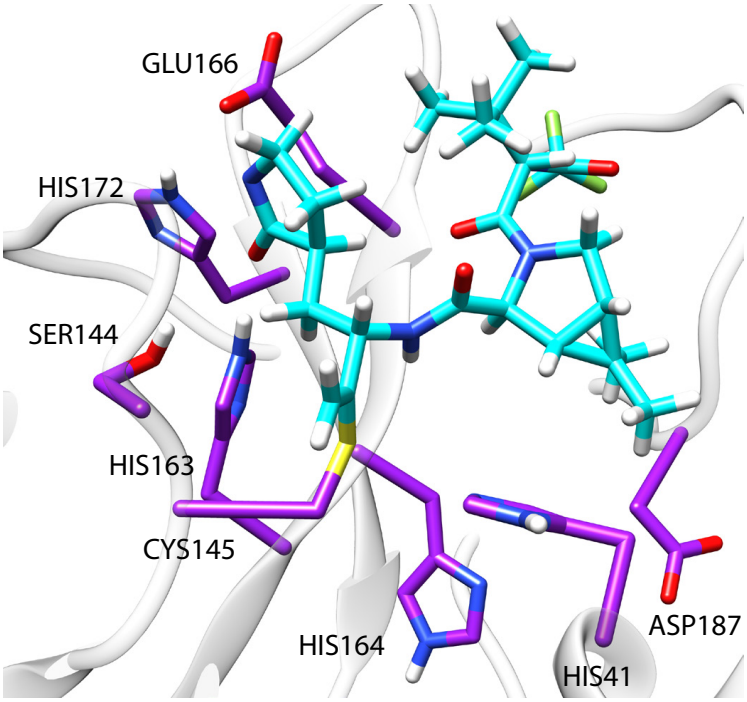

Figure 2: Structure of M^{pro} covalently bound with the alkyne derivative of nirmatrelvir (PDB 8FY6). Surrounding key residues for binding and catalytic activity are also shown. The binding pose and the conformers of the catalytic residue are essentially identical to the structure of M^{pro} covalently bound with nirmatrelvir (PDB 7RFS).

Ab Initio Calculations

As a starting point, we explored potential reaction pathways for the covalent binding of nitrile and alkyne functional groups to cysteine in a solution phase. These pathways will serve as reference reactions for our subsequent EVB calculations in water. We delineated each reaction pathway into two primary steps: a proton transfer between a cysteine and a histidine residue, and a concerted mechanism involving a proton transfer coupled with a nucleophilic attack (PT-NA), which can occur directly or with solvent assistance (see Figure 3).

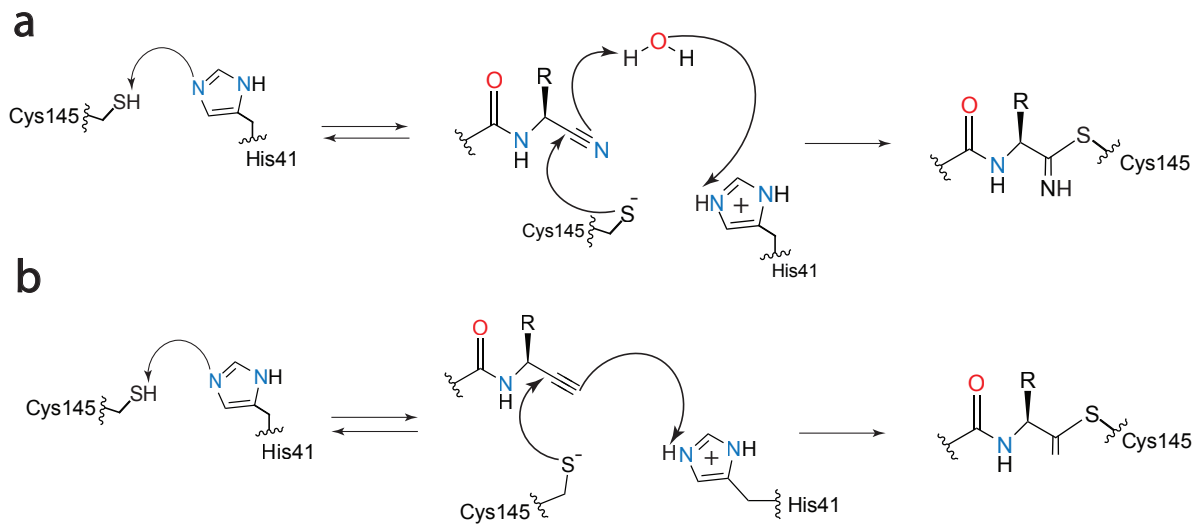

Figure 3: Reaction mechanisms for (a) nirmatrelvir and (b) its alkyne-substituted derivative. We examine a solvent-assisted concerted proton transfer-nucleophilic attack step for nitrile group of nirmatrelvir, while for the alkyne group we examine a direct mechanism.

The calibration of the EVB simulations was informed by these mechanistic explorations, as detailed in Figure S3. Our attempt to identify the transition state for a water-assisted mechanism for the alkyne group proved unsuccessful. However, we do not expect the absence of this pathway to significantly affect the energy barrier. This is based on the assumption that the non-polar nature of the alkyne group most likely hinders the introduction of water, unlike the polar nitrile group, which showed a lower energy barrier with a water-assisted mechanism compared to a direct mechanism (*vide infra*). We also investigated alternate possible mechanism involving the role of Asp187 in stabilizing the transition state. This mechanism, however, was found to be insufficiently endothermic to validate the proposed Cys145-His41-Asp187 catalytic triad hypothesis.[45]

As a result of these findings, we focused on a direct PT-NA mechanism for the alkyne group. In contrast, for the nitrile group, attention was directed towards a mechanism facilitated by water, as depicted in Figure 3. Alternative mechanisms, including those involving Asp187 and the potential catalytic triad, are illustrated in Figure S4 for further reference.

EVB Calculations

As detailed above, the ab initio calibrated EVB Hamiltonian for the reaction in solution provides the basis for modeling the corresponding enzymatic reactions. The calibrated EVB parameters as well as a summary of the reaction routes that were explored by EVB simulation are given in the Supporting Information. Each step was evaluated in a reverse order, starting from the available corresponding structures for the covalent form of the ligand, and we specifically focus on direct PT-NA mechanism for the considered warhead. In Figure 4, we present the EVB free energy profile in protein as well as the reference reaction in water for nirmatrelvir, whereas that for the alkyne derivative are depicted in Figure 5. The PT-NA step emerged as the kinetic bottleneck for both inhibitors, presenting a reaction barrier ($\Delta G^{\ddagger}$) of 17.5 kcal/mol, which corresponds to an inactivation rate constant (k_{inact}), of the order of 1 s^{-1}. This finding is in agreement with a $\Delta G^{\ddagger}$ predicted by another QM/MM approach, which posits a 16.3 kcal/mol barrier ($k_{\mathrm{inact}} \approx 10\ \mathrm{s}^{-1}$) for the nitrile group, with a lower exothermicity. [46]

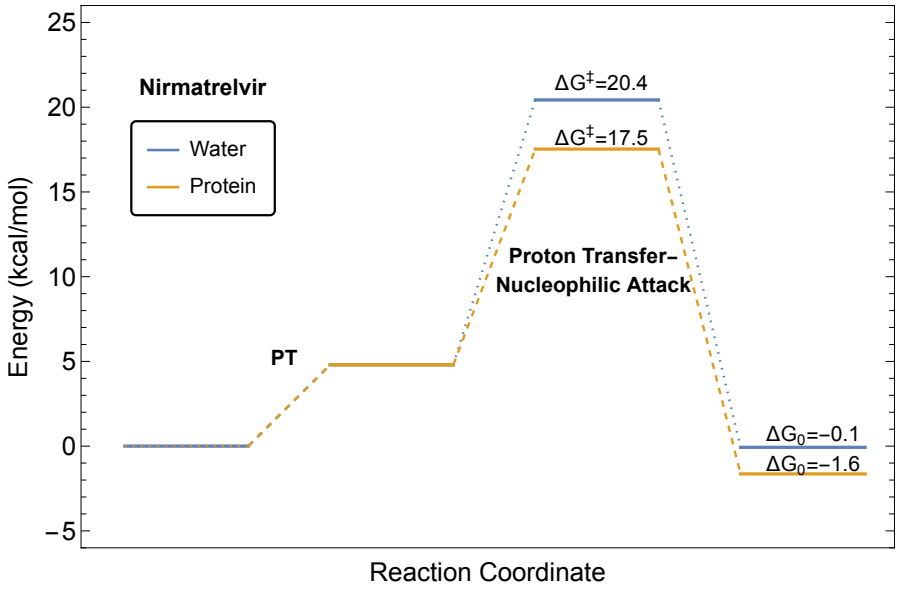

Figure 4: EVB profile for the reaction mechanism of nirmatrelvir, showing that the active site reduces the barrier of the same reaction in water by about 3 kcal/mol and essentially no exothermicity.

Similarly, for the alkyne group, the PT-NA step is the rate-limiting step, presenting an energy barrier of 20.8 kcal/mol and a correspondingly slow inactivation ($k_{\mathrm{inact}} \approx 0.01\ s^{-1}$). This reaction

step is notably exothermic and irreversible, with a substantial reaction free energy (ΔG_0) of -40 kcal/mol. For the overall reaction, the activation energy $\Delta G^{\ddagger}$ for the alkyne group is quantified at 22.7 kcal/mol, and the reaction results in ΔG_0 of -35 kcal/mol.

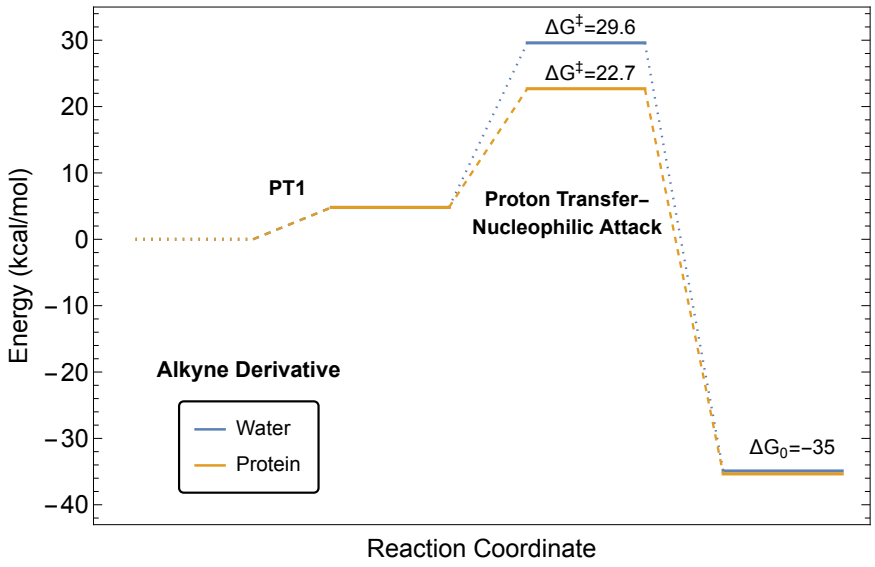

Figure 5: EVB profile for the reaction mechanism of the nirmatrelvir alkyne derivative, which has a higher barrier in protein and significant exothermicity, approximately 35 kcal/mol in both water and protein.

Kinetics Simulation of Inhibitor Selectivity

At this point, we must deal with the task of connecting the estimated and observed kinetics. We approach this task using a similar kinetics simulation approach to the strategy we developed previously in the study of the irreversible inhibition of tyrosine kinases.[35] In general, we can expect that IC50 and K_i are connected in the situation of reversible inhibitor binding. However, here we have two different reactions: one with an extremely exothermic and irreversible reaction, and another that has smaller exothermicity and is reversible. As a result, it is ideal to use the calculated reaction free-energy profiles and kinetic simulations to replicate the experimental observable, which is the time-dependent IC50(t). This should be done in addition to comparing the value of $k_{\text{eff}} = k_{\text{inact}}/K_i$, as implied by the binding energies and reaction rates.

We used a simple competitive inhibition scheme to generate the trend of the experimentally observed kinetics. The inhibition assay was simulated, subjecting the enzyme to pre-incubation with the inhibitor for a certain amount of time, and then calculating the initial velocity of product formation upon adding the substrate to the assay. We used the same initial conditions as the assay used by Zhang and co-workers[20] ($[S]_0 = 20$ μM and $[E]_0 = 0.5$ μM). In addition, the initial conditions for the alkyne derivative were taken as $[S]_0 = 20$ μM and $[E]_0 = 0.5$ μM. Additional simulation details and assay-dependent parameters are listed in the Supplementary Information. Table 1 lists the calculated kinetic and thermodynamic parameter along with simulated and experimental IC50 values. Our analysis yielded binding affinities of ΔG_{bind} = -7.5 kcal/mol for nirmatrelvir and $\Delta G_{\text{bind}} = -9.7$ kcal/mol for its alkyne derivative from our PDLD/S-LRA/β calculations (additional information on the binding energy calculations can be found in the SI).

Table 1: Summary of calculated energetics and simulated IC50 values, compared with experimental IC50 values.[20] Energies are in kcal/mol while IC50 values are in μM.

Compound	EVB		PDLD	Simulated IC50			Experimental IC50		
	$\Delta G^{\ddagger}$	ΔG_0	ΔG_{bind}	30s	15min	3h	0h	15min	3h
Nirmatrelvir	17.5	-1.6	-7.5	22	1.0	0.5	0.34 ± 0.11	0.56 ± 0.32	0.76 ± 0.27
Alkyne-Deriv.	22.7	-35	-9.7	22	0.9	0.3	15.72 ± 7.29	0.30 ± 0.12	0.063 ± 0.015

The simulated time-dependent IC50 curves are shown in Figure 6. The IC50(t) of both nirmatrelvir and its alkyne derivative is predicted to be 250 nM after 3 hours of pre-incubation. However, the alkyne derivative initially has a much larger IC50 (10 μM) without any preincubation. The experimental value of k_{eff} for the alkyne inhibitor[20] is 5.3×10^7 $\text{M}^{-1}\text{s}^{-1}$ while the calculated k_{eff} value based on our EVB and binding affinity calculations is 2.3×10^5 $\text{M}^{-1}\text{s}^{-1}$. The deviation between the experimental and predicted IC50 likely originates from a discrepancy in the binding affinity, which may be in part due to the experimental relative error. It is also possible that PDLD/S-LRA/β is underestimating the binding energy of the inhibitors. Measurements of K_i of these inhibitors at higher precision would help to clarify the issue.

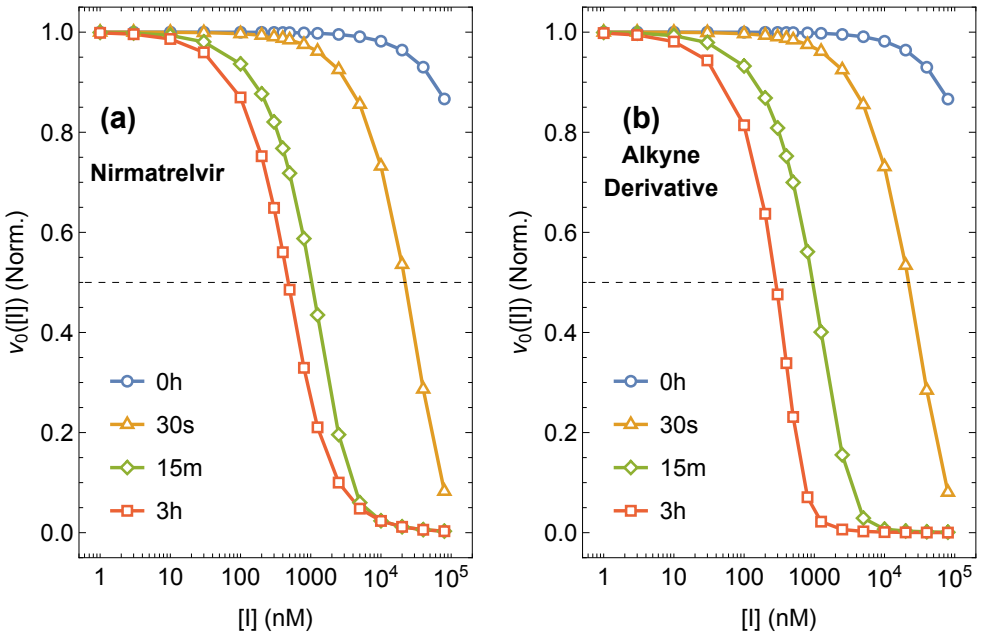

Figure 6: Simulated incubation assay of M^{pro} under different preincubation times with the inhibitors, nirmatrelvir (a) and its alkyne derivative (b). The IC50 is obtained as the inhibitor concentration for which the velocity of product formation is cut by 50% (dashed line). The irreversibility of the reaction with the alkyne warhead is apparent by strong dependence of the IC50 on pre-incubation time.

Conclusions

The main protease (M^{pro}) of the coronavirus, a cysteine protease featuring a Cys145-His41 catalytic dyad, is essential for viral replication and the subsequent infection in humans. The present study builds on the existing body of work on SARS-CoV-2 M^{pro} inhibitors, highlighting covalent inhibition as a particularly promising strategy in the development of antiviral drugs. Specifically, the inhibitors nirmatrelvir and its analogs can act on M^{pro} either reversibly or irreversibly to obstruct the virus's lifecycle.

Our investigation delved into the thermodynamics of inhibition by two distinct inhibitors, each characterized by different reactive groups i.e., one bearing a nitrile group and the other an alkyne group. By employing both EVB and PDLD/S-LRA/β simulations, we were able to delineate the

binding energetics associated with both covalent and non-covalent interactions of these compounds. The insights from our kinetic modeling, detailed in Table 1, align with experimental data and notably reveal the superior efficacy of the alkyne-modified inhibitor over a duration of three hours. Nonetheless, to reconcile certain qualitative deviations observed at shorter intervals, further experiments with reduced relative errors are necessary. A point of ongoing inquiry is the precise binding affinities of nirmatrelvir and its derivatives. The study notes that the binding affinity is subject to significant variation depending on the tautomeric form of HIS163; however, no other histidine residue has been found to exert a comparable influence.

In conclusion, while there remains room for refinement in our results, it is important to acknowledge the contribution of our work in simulating the time-dependent potency of covalent inhibitors. This approach, as exemplified in the context of M^{pro} inhibitors, promises to be a valuable tool in the identification and subsequent pharmaceutical assessment of potential lead compounds.

Data Availability

Optimized and transition state ab initio structures used for the EVB reference reactions are available at https://github.com/Mojgan-Asadi/mpro-ab-initio.

Acknowledgments

This work was supported by the National Institutes of Health R35 GM122472 and the National Science Foundation Grant MCB 2142727.

References:

(1) Gajjar, N. D.; Dhameliya, T. M.; Shah, G. B. In Search of RdRp and Mpro Inhibitors against SARS CoV-2: Molecular Docking, Molecular Dynamic Simulations and ADMET Analysis. *J. Mol. Struct.* **2021**, *1239*, 130488. https://doi.org/10.1016/j.molstruc.2021.130488.
(2) Gao, X.; Qin, B.; Chen, P.; Zhu, K.; Hou, P.; Wojdyla, J. A.; Wang, M.; Cui, S. Crystal Structure of SARS-CoV-2 Papain-like Protease. *Acta Pharm. Sin. B* **2021**, *11* (1), 237–245. https://doi.org/10.1016/j.apsb.2020.08.014.
(3) Silva, L. R.; da Silva Santos-Júnior, P. F.; de Andrade Brandão, J.; Anderson, L.; Bassi, Ê. J.; Xavier de Araújo-Júnior, J.; Cardoso, S. H.; da Silva-Júnior, E. F. Druggable Targets

from Coronaviruses for Designing New Antiviral Drugs. *Bioorg. Med. Chem.* **2020**, *28* (22), 115745. https://doi.org/10.1016/j.bmc.2020.115745.
(4) Dai, W.; Zhang, B.; Jiang, X.-M.; Su, H.; Li, J.; Zhao, Y.; Xie, X.; Jin, Z.; Peng, J.; Liu, F.; Li, C.; Li, Y.; Bai, F.; Wang, H.; Cheng, X.; Cen, X.; Hu, S.; Yang, X.; Wang, J.; Liu, X.; Xiao, G.; Jiang, H.; Rao, Z.; Zhang, L.-K.; Xu, Y.; Yang, H.; Liu, H. Structure-Based Design of Antiviral Drug Candidates Targeting the SARS-CoV-2 Main Protease. *Science* **2020**, *368* (6497), 1331–1335. https://doi.org/10.1126/science.abb4489.
(5) Ullrich, S.; Nitsche, C. The SARS-CoV-2 Main Protease as Drug Target. *Bioorg. Med. Chem. Lett.* **2020**, *30* (17), 127377. https://doi.org/10.1016/j.bmcl.2020.127377.
(6) Mengist, H. M.; Dilnessa, T.; Jin, T. Structural Basis of Potential Inhibitors Targeting SARS-CoV-2 Main Protease. *Front. Chem.* **2021**, *9*.
(7) Ziebuhr, J.; Herold, J.; Siddell, S. G. Characterization of a Human Coronavirus (Strain 229E) 3C-like Proteinase Activity. *J. Virol.* **1995**, *69* (7), 4331–4338. https://doi.org/10.1128/jvi.69.7.4331-4338.1995.
(8) Poduri, R.; Joshi, G.; Jagadeesh, G. Drugs Targeting Various Stages of the SARS-CoV-2 Life Cycle: Exploring Promising Drugs for the Treatment of Covid-19. *Cell. Signal.* **2020**, *74*, 109721. https://doi.org/10.1016/j.cellsig.2020.109721.
(9) Gao, K.; Wang, R.; Chen, J.; Tepe, J. J.; Huang, F.; Wei, G.-W. Perspectives on SARS-CoV-2 Main Protease Inhibitors. *J. Med. Chem.* **2021**, *64* (23), 16922–16955. https://doi.org/10.1021/acs.jmedchem.1c00409.
(10) Gimeno, A.; Mestres-Truyol, J.; Ojeda-Montes, M. J.; Macip, G.; Saldivar-Espinoza, B.; Cereto-Massagué, A.; Pujadas, G.; Garcia-Vallvé, S. Prediction of Novel Inhibitors of the Main Protease (M-pro) of SARS-CoV-2 through Consensus Docking and Drug Reposition. *Int. J. Mol. Sci.* **2020**, *21* (11), 3793.
(11) Tuley, A.; Fast, W. The Taxonomy of Covalent Inhibitors. *Biochemistry* **2018**, *57* (24), 3326–3337. https://doi.org/10.1021/acs.biochem.8b00315.
(12) Mestres, J.; Gregori-Puigjané, E.; Valverde, S.; Solé, R. V. The Topology of Drug–Target Interaction Networks: Implicit Dependence on Drug Properties and Target Families. *Mol. Biosyst.* **2009**, *5* (9), 1051–1057. https://doi.org/10.1039/B905821B.
(13) Singh, J.; Petter, R. C.; Baillie, T. A.; Whitty, A. The Resurgence of Covalent Drugs. *Nat. Rev. Drug Discov.* **2011**, *10* (4), 307–317. https://doi.org/10.1038/nrd3410.
(14) Banerjee, R.; Perera, L.; Tillekeratne, L. V. Potential SARS-CoV-2 Main Protease Inhibitors. *Drug Discov. Today* **2021**, *26* (3), 804–816.
(15) Al-Khafaji, K.; AL-DuhaidahawiL, D.; Taskin Tok, T. Using Integrated Computational Approaches to Identify Safe and Rapid Treatment for SARS-CoV-2. *J. Biomol. Struct. Dyn.* **2020**, 1–9. https://doi.org/10.1080/07391102.2020.1764392.
(16) Tung Ngo, S.; Hai Nguyen, T.; Thanh Tung, N.; Khanh Mai, B. Insights into the Binding and Covalent Inhibition Mechanism of PF-07321332 to SARS-CoV-2 M Pro. *RSC Adv.* **2022**, *12* (6), 3729–3737. https://doi.org/10.1039/D1RA08752E.
(17) Paul, A. S.; Islam, R.; Parves, M. R.; Mamun, A. A.; Shahriar, I.; Hossain, M. I.; Hossain, M. N.; Ali, M. A.; Halim, M. A. Cysteine Focused Covalent Inhibitors against the Main Protease of SARS-CoV-2. *J. Biomol. Struct. Dyn.* **2022**, *40* (4), 1639–1658. https://doi.org/10.1080/07391102.2020.1831610.
(18) Mondal, D.; Warshel, A. Exploring the Mechanism of Covalent Inhibition: Simulating the Binding Free Energy of α-Ketoamide Inhibitors of the Main Protease of SARS-CoV-2. *Biochemistry* **2020**, *59* (48), 4601–4608. https://doi.org/10.1021/acs.biochem.0c00782.

(19) Cokley, J. A.; Gidal, B. E.; Keller, J. A.; Vossler, D. G. PaxlovidTM Information From FDA and Guidance for AES Members. *Epilepsy Curr.* **2022**, *22* (3), 201–204. https://doi.org/10.1177/15357597221088415.
(20) Ngo, C.; Fried, W.; Aliyari, S.; Feng, J.; Qin, C.; Zhang, S.; Yang, H.; Shanaa, J.; Feng, P.; Cheng, G.; Chen, X. S.; Zhang, C. Alkyne as a Latent Warhead to Covalently Target SARS-CoV-2 Main Protease. *J. Med. Chem.* **2023**, *66* (17), 12237–12248. https://doi.org/10.1021/acs.jmedchem.3c00810.
(21) Zhou, J.; Saha, A.; Huang, Z.; Warshel, A. Fast and Effective Prediction of the Absolute Binding Free Energies of Covalent Inhibitors of SARS-CoV-2 Main Protease and 20S Proteasome. *J. Am. Chem. Soc.* **2022**, *144* (17), 7568–7572. https://doi.org/10.1021/jacs.2c00853.
(22) Brewitz, L.; Dumjahn, L.; Zhao, Y.; Owen, C. D.; Laidlaw, S. M.; Malla, T. R.; Nguyen, D.; Lukacik, P.; Salah, E.; Crawshaw, A. D.; Warren, A. J.; Trincao, J.; Strain-Damerell, C.; Carroll, M. W.; Walsh, M. A.; Schofield, C. J. Alkyne Derivatives of SARS-CoV-2 Main Protease Inhibitors Including Nirmatrelvir Inhibit by Reacting Covalently with the Nucleophilic Cysteine. *J. Med. Chem.* **2023**, *66* (4), 2663–2680. https://doi.org/10.1021/acs.jmedchem.2c01627.
(23) Tan, B.; Sacco, M.; Tan, H.; Li, K.; Joyce, R.; Zhang, X.; Chen, Y.; Wang, J. Exploring Diverse Reactive Warheads for the Design of SARS-CoV-2 Main Protease Inhibitors. *Eur. J. Med. Chem.* **2023**, *259*, 115667. https://doi.org/10.1016/j.ejmech.2023.115667.
(24) Owen, D. R.; Allerton, C. M.; Anderson, A. S.; Aschenbrenner, L.; Avery, M.; Berritt, S.; Boras, B.; Cardin, R. D.; Carlo, A.; Coffman, K. J. An Oral SARS-CoV-2 Mpro Inhibitor Clinical Candidate for the Treatment of COVID-19. *Science* **2021**, *374* (6575), 1586–1593.
(25) Van Der Spoel, D.; Lindahl, E.; Hess, B.; Groenhof, G.; Mark, A. E.; Berendsen, H. J. C. GROMACS: Fast, Flexible, and Free. *J. Comput. Chem.* **2005**, *26* (16), 1701–1718. https://doi.org/10.1002/jcc.20291.
(26) Maple, J. R.; Dinur, U.; Hagler, A. T. Derivation of Force Fields for Molecular Mechanics and Dynamics from Ab Initio Energy Surfaces. *Proc. Natl. Acad. Sci.* **1988**, *85* (15), 5350–5354. https://doi.org/10.1073/pnas.85.15.5350.
(27) Frisch, M. ea; Trucks, G. W.; Schlegel, H. B.; Scuseria, G. E.; Robb, M. A.; Cheeseman, J. R.; Scalmani, G.; Barone, V.; Petersson, G. A.; Nakatsuji, H. Gaussian 16, 2016.
(28) Zhao, Y.; Truhlar, D. G. The M06 Suite of Density Functionals for Main Group Thermochemistry, Thermochemical Kinetics, Noncovalent Interactions, Excited States, and Transition Elements: Two New Functionals and Systematic Testing of Four M06-Class Functionals and 12 Other Functionals. *Theor. Chem. Acc.* **2008**, *120* (1), 215–241. https://doi.org/10.1007/s00214-007-0310-x.
(29) Francl, M. M.; Pietro, W. J.; Hehre, W. J.; Binkley, J. S.; Gordon, M. S.; DeFrees, D. J.; Pople, J. A. Self-consistent Molecular Orbital Methods. XXIII. A Polarization-type Basis Set for Second-row Elements. *J. Chem. Phys.* **1982**, *77* (7), 3654–3665. https://doi.org/10.1063/1.444267.
(30) McLean, A. D.; Chandler, G. S. Contracted Gaussian Basis Sets for Molecular Calculations. I. Second Row Atoms, Z=11–18. *J. Chem. Phys.* **1980**, *72* (10), 5639–5648. https://doi.org/10.1063/1.438980.
(31) Spitznagel, G. W.; Clark, T.; von Ragué Schleyer, P.; Hehre, W. J. An Evaluation of the Performance of Diffuse Function-Augmented Basis Sets for Second Row Elements, Na-Cl. *J. Comput. Chem.* **1987**, *8* (8), 1109–1116. https://doi.org/10.1002/jcc.540080807.

(32) Barone, V.; Cossi, M. Quantum Calculation of Molecular Energies and Energy Gradients in Solution by a Conductor Solvent Model. *J. Phys. Chem. A* **1998**, *102* (11), 1995–2001. https://doi.org/10.1021/jp9716997.
(33) Warshel, A.; Weiss, R. M. An Empirical Valence Bond Approach for Comparing Reactions in Solutions and in Enzymes. *J. Am. Chem. Soc.* **1980**, *102* (20), 6218–6226. https://doi.org/10.1021/ja00540a008.
(34) Kamerlin, S. C. L.; Warshel, A. The Empirical Valence Bond Model: Theory and Applications. *WIREs Comput. Mol. Sci.* **2011**, *1* (1), 30–45. https://doi.org/10.1002/wcms.10.
(35) Asadi, M.; Xie, W. J.; Warshel, A. Exploring the Role of Chemical Reactions in the Selectivity of Tyrosine Kinase Inhibitors. *J. Am. Chem. Soc.* **2022**, *144* (36), 16638–16646.
(36) Oanca, G.; Asadi, M.; Saha, A.; Ramachandran, B.; Warshel, A. Exploring the Catalytic Reaction of Cysteine Proteases. *J. Phys. Chem. B* **2020**, *124* (50), 11349–11356. https://doi.org/10.1021/acs.jpcb.0c08192.
(37) Tandarić, T.; Prah, A.; Stare, J.; Mavri, J.; Vianello, R. Hydride Abstraction as the Rate-Limiting Step of the Irreversible Inhibition of Monoamine Oxidase B by Rasagiline and Selegiline: A Computational Empirical Valence Bond Study. *Int. J. Mol. Sci.* **2020**, *21* (17), 6151. https://doi.org/10.3390/ijms21176151.
(38) Prah, A.; Purg, M.; Stare, J.; Vianello, R.; Mavri, J. How Monoamine Oxidase A Decomposes Serotonin: An Empirical Valence Bond Simulation of the Reactive Step. *J. Phys. Chem. B* **2020**, *124* (38), 8259–8265.
(39) Bauer, P.; Barrozo, A.; Purg, M.; Amrein, B. A.; Esguerra, M.; Wilson, P. B.; Major, D. T.; Åqvist, J.; Kamerlin, S. C. L. Q6: A Comprehensive Toolkit for Empirical Valence Bond and Related Free Energy Calculations. *SoftwareX* **2018**, *7*, 388–395. https://doi.org/10.1016/j.softx.2017.12.001.
(40) Mark, P.; Nilsson, L. Structure and Dynamics of the TIP3P, SPC, and SPC/E Water Models at 298 K. *J. Phys. Chem. A* **2001**, *105* (43), 9954–9960. https://doi.org/10.1021/jp003020w.
(41) King, G.; Warshel, A. A Surface Constrained All-atom Solvent Model for Effective Simulations of Polar Solutions. *J. Chem. Phys.* **1989**, *91* (6), 3647–3661. https://doi.org/10.1063/1.456845.
(42) Lee, F. S.; Warshel, A. A Local Reaction Field Method for Fast Evaluation of Long-range Electrostatic Interactions in Molecular Simulations. *J. Chem. Phys.* **1992**, *97* (5), 3100–3107. https://doi.org/10.1063/1.462997.
(43) Warshel, A. *Computer Modeling of Chemical Reactions in Enzymes and Solutions*; Wiley: New York, 1991.
(44) Singh, N.; Warshel, A. Absolute Binding Free Energy Calculations: On the Accuracy of Computational Scoring of Protein–Ligand Interactions. *Proteins Struct. Funct. Bioinforma.* **2010**, *78* (7), 1705–1723. https://doi.org/10.1002/prot.22687.
(45) Nguyen, T. H.; Tam, N. M.; Van Tuan, M.; Zhan, P.; Vu, V. V.; Quang, D. T.; Ngo, S. T. Searching for Potential Inhibitors of SARS-COV-2 Main Protease Using Supervised Learning and Perturbation Calculations. *Chem. Phys.* **2023**, *564*, 111709.
(46) Ramos-Guzmán, C. A.; Ruiz-Pernía, J. J.; Tuñón, I. Computational Simulations on the Binding and Reactivity of a Nitrile Inhibitor of the SARS-CoV-2 Main Protease. *Chem. Commun.* **2021**, *57* (72), 9096–9099. https://doi.org/10.1039/D1CC03953A.